

Monodisperse Carbon Nitride Nanosheets as Multifunctional Additives for Efficient and Durable Perovskite Solar Cells

Dae-won Kim[†], Jungwoo Choi[‡], Jinwoo Byun[†], Jun Tae Kim[†], Gang San Lee[†], Jin Goo Kim[†],

Daehan Kim[‡], Passarut Boonmongkolras[‡], Paul F. McMillan[#], Hyuck Mo Lee[‡], Adam J. Clancy^{#,}*

Byungha Shin^{#} and Sang Ouk Kim^{†*}*

[†] National Creative Research Initiative Center for Multi-Dimensional Directed Nanoscale Assembly, Department of Material Science and Engineering, Korea Advanced Institute of Science and Technology (KAIST), Daejeon 34141, Republic of Korea,

[‡] Department of Material Science and Engineering, Korea Advanced Institute of Science and Technology (KAIST), Daejeon 34141, Republic of Korea

[#] Department of Chemistry, University College London (UCL), Gower St., London WC1E 6BT, United Kingdom

Corresponding Author

* Corresponding Author: Adam J. Clancy (email: a.clancy@ucl.ac.uk), Byungha Shin (email: byungha@kaist.ac.kr), Sang Ouk Kim (email: sangouk.kim@kasit.ac.kr)

Abstracts

2D materials are promising components for defect passivation of metal halide perovskites. Unfortunately, commonly used polydisperse liquid-exfoliated 2D materials generally suffer from heterogeneous structures and properties while incorporated into perovskite films. We introduce monodisperse multifunctional 2D crystalline carbon nitride, poly(triazine imide) (PTI), as an effective defect passivation agent in perovskite films via typical solution processing. Incorporation of PTI into perovskite film can be readily attained by simple solution mixing of PTI dispersions with perovskite precursor solutions, resulting in the highly selective distribution of PTI localized at the defective crystal grain boundaries and layer interfaces in the functional perovskite layer. Several chemical, optical and electronic characterization, in conjunction with density-functional theory calculations, reveals multiple beneficial roles from PTI: passivation of undercoordinated organic cations at the surface of perovskite crystal, suppression of ion migration by blocking diffusion channels and prevention of hole quenching at perovskite/SnO₂ interfaces. Consequently, noticeably improved power conversion efficiency is achieved in perovskite solar cells, accompanied with promoted stability under humid air and thermal stress. Our strategy highlights the potential of judiciously designed 2D materials as a simple-to-implement material for various optoelectronic devices, including solar cells, based on hybrid perovskites.

Keywords: Metal halide perovskites, Solar cells, 2D materials, Defects passivation, Poly(triazine imide)

Introduction

Metal halide perovskites have emerged as promising materials for solar cells,¹⁻³ light-emitting diodes,^{4,6} transistors,⁷ and sensors.⁸ Noticeably, metal halide perovskite solar cells (PSCs) have achieved rapid, unprecedented advance in the power conversion efficiencies (PCEs) approaching 25.5%.⁹ Unfortunately, typical solution processing of perovskite relying on the relatively weak and vulnerable inter-elemental binding yields a high density of crystal defects, such as undercoordinated ions or halide vacancy sites.¹⁰ These defects are predominantly formed at the periodic perovskite lattice termination (i.e. interfaces and grain boundaries), upon the evaporation of volatile components¹¹ or atomistic reorganization at the crystalline surfaces.¹² Such crystal defects in perovskite commonly yield electronic trap states that can induce non-radiative recombination, significantly reducing PCEs. Moreover, vacancy defects also offer leakage pathways for ion migration along the grain boundaries and thus deteriorate the reliability and long-term stability of PSCs.¹³

Undesirable defect states in perovskites can be passivated by introducing additives, to date, including salts,¹⁴ organic molecules,¹⁵ quantum dots,¹⁶ polymers¹⁷ and two-dimensional (2D) materials¹⁸ particularly targeting the interfaces and grain boundaries. These passivation agents can

form hydrogen or coordination bonding with adjacent perovskite crystals to passivate the undercoordinated sites that are prone to defect formation.¹⁹⁻²¹ In particular, 2D materials are ideal passivation agents to enhance the photophysical properties of perovskites, as the dense surface functionalities intrinsic to 2D materials facilitate the intimate binding with perovskite crystals, thereby stabilizing the defective interfaces and grain boundaries in perovskite films. Furthermore, inherent planar structure of 2D materials can effectively block or retard the out-diffusion of mobile species from perovskite crystals, to enhance environmental stability.²² To date, several different 2D materials, including graphene oxide,²³ transition metal dichalcogenides (MoS₂, WS₂)^{24, 25} MXenes (Ti₃C₂T_x)^{26, 27} have been employed for efficient and durable PSCs.

Highly crystalline 2D semiconductor, poly(triazine imide) (PTI) is composed of triazine moieties linked by imide bridges.²⁸ In contrast to typical thermolytic carbon nitrides, consisting of partially cross-linked polymeric heptazine-based chains, PTI is synthesized under high pressure or in molten salts, leading to the formation of discrete 2D crystals held together by van der Waals forces.²⁹ Significantly, monolayer level dissolution of PTI sheets is spontaneous in select polar aprotic solvents such as dimethyl sulfoxide (DMSO) and *N,N*-dimethylformamide (DMF) without sonication, while avoiding sonochemical damage to the planar crystalline structure.^{30, 31} This new class of synthetic 2D materials is appealing for catalytic and membrane applications taking advantage of its novel electronegative cavities, high chemical and thermal robustness, and unique dissolution characteristics.^{30, 32, 33}

In this work, we introduce PTI as an ideal defect passivation agent for metal halide perovskites, to effectively improve the device performance and environmental stability of PSCs. Unlike typical liquid-exfoliated 2D materials of non-uniform stacking numbers and lateral dimensions, which generically result in heterogeneous material structures and properties,^{34, 35} monodisperse PTI nanosheets demonstrate a well-defined spatial distribution selectively localized at the defective interfaces and grain boundaries, throughout the perovskite layer thickness. As such, PTI nanosheets with dense electronegative functionalities successfully passivate the defective perovskite crystalline structure and interfaces with the minimal disturbance of original high crystalline nature.

Results and Discussion

PTI bulk crystals were prepared by the condensation of dicyandiamide in a molten eutectic LiBr/KBr salt bath, forming the stacks of 2D PTI intercalated with LiBr, which was subsequently washed by Soxhlet extraction with water.³⁶ The hexagonal 2D planar structure of PTI with a $C_6N_9H_3$ stoichiometry consist of 1,3,5-triazine ring linked via three bridging N-H units (Figure S1).³³ PTI nanosheets were exfoliated in a 4:1 (v/v) mixture of DMF and DMSO, taking advantage of the inherent good solubility (Figure 1a).³⁰ The well-exfoliated morphology of PTI was confirmed by atomic force microscopy (AFM) and transmission electron microscopy (TEM) (Figure S2). Highly crystalline 2D PTI nanosheets are observed with narrow lateral (54.0 ± 14.1 nm) and thickness (1.02 ± 0.33 nm, about 3 layers) distributions, dramatically more homogeneous than other typical liquid-exfoliated 2D materials of polydisperse size and shape.³⁷⁻³⁹ While the electronic band structure of 2D materials is strongly influenced by surface defects, lateral size and layer number,^{34, 35} our single-crystalline domain, monodisperse PTI offers highly uniform

electronic properties with a high reliability. The prepared PTI dispersions were directly mixed with perovskite precursor solutions without any solvent incompatibility or aggregation problem (Figure S3). Various precursor solutions with different composition of PTI were prepared, and the resultant perovskite films are denoted as PTI-x, indicating x μg of PTI in 1 ml perovskite precursor solution (a pristine perovskite film without PTI is denoted as reference).

Figure 1b schematically illustrates the PTI-incorporated PSCs consisting of triple cation, double halide perovskite layer of $\text{Cs}_{0.05}(\text{FA}_{0.83}\text{MA}_{0.17})_{0.95}\text{Pb}(\text{I}_{0.83}\text{Br}_{0.17})_3$ (FA^+ = formamidinium = $\text{CH}(\text{NH}_2)_2^+$; MA^+ = methylammonium = CH_3NH_3^+) with the n-i-p planar structure of ITO/SnO₂/perovskite:PTI/Spiro-OMeTAD/Au. Owing to the uniform nanoscale size, PTI is readily excluded from the bulk of perovskite crystal during the nucleation and growth, precipitating at the interfaces and grain boundaries of polycrystalline domains. Electronegative nitrogen atoms in the triazine ring and imide group of PTI can interact with the undercoordinated surface FA^+ or MA^+ on perovskite crystals by hydrogen bonding (*vide infra*).

We conducted TEM analysis for the detection of PTI sheets within perovskite layers. PTI nanosheets with well-defined edges are apparent without interfering the crystalline perovskite lattices (Figure 1c and S4). Figure 1d shows a magnified TEM image from the red dashed region in Figure 1c as well as the corresponding fast Fourier transform (inset image). The hexagonal symmetry of PTI and interplanar spacings are evident, which match well with the (200) and (220) of PTI bulk crystal, verifying the successful incorporation of PTI without any physical/chemical damage.^{30, 33} We performed time-of-flight secondary ion mass spectrometry (ToF-SIMS) to further

identify the spatial distribution of PTI in the perovskite films. Argon gas cluster ion beam was used to minimize ion sputtering induced damage (Figure 1e). A signal at $m/z = 90$ from the PTI bulk powder is attributed to $C_4N_3^-$ (Figure S5), which is detected at a higher intensity in PTI-60 compared to PTI-30, but virtually absent for the PTI-free reference with a trace signal attributed to C/N-containing perovskite organic components (FA^+ , MA^+). As such, the spatial distribution of PTI was traced by following the $C_4N_3^-$ signal trend, alongside the signals assigned to perovskite (PbI^- , I_2^-) and tin oxide (SnO_2^-) to monitor relative compositional change as a function of penetrating depth in the film thickness direction. The PTI is found to be gradually distributed throughout the entire film thickness, while predominantly accumulates at the buried perovskite/ SnO_2 interface.

To monitor the influence of PTI on the charge transport properties, we performed vertical dark J-V measurements on ITO/perovskite/Au devices (Figure 2a). In PTI-15 and PTI-30, there is a modest decrease in the vertical conductivity, while a significant drop is observed for PTI-60. This trend can be understood by the retarded inter-grain charge transport and/or increase in the contact resistance between the perovskite layer and substrate by the localized distribution of wide band gap PTI (~ 3.2 eV, Figure S6). However, perovskite crystalline structure, morphology, and band gap (~ 1.63 eV) are not noticeably modified by the presence of PTI, as shown in Figure 2b for X-ray diffraction (XRD), Figure S7 for ultraviolet-visible (UV-vis), and Figure S8 for absorption spectroscopy and scanning electron microscopy (SEM).⁴⁰

While the structure and morphology of perovskite layer remained unaltered with the addition of PTI, notably distinct the optical properties and charge carrier dynamics were observed depending on the PTI concentration. The steady-state photoluminescence (PL) intensity measured with a 633 nm excitation laser became stronger with the increasing PTI composition (Figure 2c and S9), suggesting the effective passivation of non-radiative defects with PTI. Moreover, compared to the reference, full-width at half maximum (FWHM) of the PL peaks became narrower in the PTI-incorporated films. This is principally due to the reduction of luminescence from the longer wavelength side (apparent blue-shift from 769 to 765 nm), also consistent with the reduction of defect states in the perovskite grain boundaries and interface.⁴¹

Figure 2d presents time-resolved PL (TRPL) measurements with a 467 nm excitation laser incident from the glass substrate side as well as from the bare perovskite surface side. The TRPL curves were fitted with a single exponential decay models to quantify the PL lifetime (Table S1).⁴² The charge carrier recombination lifetime significantly increases with the addition of PTI in both surface-side and glass-side illumination, indicating the reduced non-radiative defect density.⁴³ Notably, the lifetime enhancement is more pronounced at the glass side where PTI is predominantly accumulated. Owing to the short penetration depth (~ 40 nm) of 467 nm laser into the perovskite film (~500 nm), TRPL spectrum is expected to be mostly influenced by shallow thickness from the surface receiving the excitation.^{44, 45} Therefore, the similar lifetimes from PTI-30 and PTI-60 indicate that the interfacial passivation by PTI already saturates by the amount used in PTI-30 and the excessive PTI would degrade the device performance by interrupting charge transport (Figure 2a). Considering the ToF-SIMS depth profiles (Figure 1e) revealing that the PTI is highly concentrated at the buried interface along with a tailing towards the surface, the gradual

increase in the PL lifetimes from the bare surface illumination can be understood by the increasing quantity of PTI near the surface along with the increase of overall incorporation.

Electronic structures of the perovskite films were examined by ultraviolet photoelectron spectroscopy (UPS) (Figure 2e). The work function (WF), determined from the secondary electron cut-off, reduces from 4.17 to 4.07 eV with the incorporation of PTI. The Fermi level (E_F) for the reference and PTI-30 are located at 1.39 and 1.51 eV above the valence band maximum (VBM), respectively. The energy level diagrams of perovskite films derived from UPS and optical absorption measurements are shown in Figure 2f. The VBM and conduction band minimum (CBM) of PTI-30 are nearly identical to the reference film; however, PTI causes the shift of WF by 100 meV toward the vacuum level (E_{vac}), while E_F shifted by 120 meV towards the CBM. This indicates that the PTI-30 films become more n-type, which is likely due to the change of the surface termination in the presence of PTI.⁴⁶⁻⁴⁸ Considering the band structure of PTI (Figure S6 and S10), it serves as a hole blocking layer at the perovskite/SnO₂ interfaces, as schematically illustrated in Figure S11.^{47, 49, 50} Point defects such as interstitial sites (Sn_i) and oxygen vacancies (V_O) are known to be formed at the surface of SnO₂ film during fabrication.^{1, 51} These defects may serve as electron trap sites and promote the detrimental interfacial recombination with holes from the perovskites. The wide band gap PTI with a large VBM energy offset suppresses such hole quenching at the interface of perovskite/SnO₂.⁵²

For a detailed molecular level understanding of the passivation effect from PTI, intermolecular interactions between organic cations in the perovskite and PTI were explored with ¹H nuclear

magnetic resonance (^1H NMR) spectroscopy (Figure 3a). In a pristine FAI solution without PTI, two peaks were detected originating from the FA^+ : the 'a' peak at 8.82 ppm from the ammonium hydrogens of FA^+ , whereas 'b' peak at 7.85 ppm from the formic hydrogen of FA^+ .⁵³ The 'a' peak became broadened in FAI dissolved in PTI dispersion and corresponding FWHM value increased to 0.065 from 0.037 for pure FAI. It clarifies that the FA^+ ammonium hydrogen atoms are influenced by the presence of PTI. A similar behavior is also observed for the MA^+ ammonium hydrogens (Figure S12).

We further confirmed the ammonium cation-PTI interaction by using attenuated total reflectance-Fourier transform infrared spectroscopy (ATR-FTIR) (Figure 3b). To improve the IR signal from PTI, samples were prepared from a low concentration perovskite precursor solution (0.01 M), i.e., a larger relative concentration of PTI. Two characteristic absorption bands are observed at 1710 and 1616 cm^{-1} from PTI-free pristine perovskite films, which can be assigned to the vibration modes of C=N and the N-H bonds from organic cations, respectively.⁵⁴ For the PTI-incorporated perovskite films, these peaks associated with C=N and N-H stretching vibrations are slightly red-shifted (to 1706 and 1608 cm^{-1} , respectively). Besides, two characteristic peaks of PTI from triazine (N=C-N, 1587 cm^{-1}) and secondary imide bridges (C-NH-C, 1444 cm^{-1}) are apparent in the PTI-incorporated perovskite film with the red-shift to 1573 and 1415 cm^{-1} respectively, compared to PTI bulk powder.^{28, 55} The ATR-FTIR results, in conjunction with ^1H NMR, suggest the formation of hydrogen bonding, $\text{N-H}\cdots\text{N}$, between the H atoms in the ammonium group of FA^+/MA^+ and the N atoms in constituent triazine and imide group of PTI. This intermolecular hydrogen bonding broadens the ^1H NMR peak by the conformational restriction of FA^+/MA^+

ions⁵⁶ and weakens the intramolecular bonding in both organic cations and PTI, while decreasing the corresponding vibrational frequency.^{17, 44, 45}

For a detailed analysis on the interfacial modification caused by PTI, DFT calculations were conducted for a cubic (100) FAPbI₃ slab (3×3×2) in the presence of a simplified PTI model consisting of a single nanopore, [C₃N₃(NH₂)NH]₆ (Figure 3c and d). We select FAI-terminated perovskite model as a typical thermodynamically stable surface state.⁵⁷ Noteworthy that, the previously reported energy level alignments of FAI-terminated perovskite are similar to our perovskite films (Figure 2f).⁵⁸ The most distinguishable change driven by PTI additive, is the reconstruction of surface outermost FA⁺ for the maximal intermolecular interaction between FA⁺ and PTI. Moreover, hydrogen bonding between the H atom of FA⁺ and the PTI is detected, which is reflected in the high binding energy, -4.22 eV, between the FAPbI₃ slab and the PTI. Interestingly, in an FAPbI₃ slab with an iodine vacancy, surface FA⁺ ions surrounding the iodine vacancy reorient themselves toward the PTI to stabilize local structure due to the loss of coordination site (Figure S13). This reorientation of FA⁺ induced by the intermolecular hydrogen bonding, while exposing electropositive ammonium group away from the surface, contributes to the surface dipole formation which is likely to cause of the WF shift probed by UPS.⁵⁸ We calculate the formation energies of FA⁺ vacancy (V_{FA}), iodine vacancy (V_I) and Pb-I antisite (Pb_I), which serve as carrier recombination and vulnerable degradation sites, at the surface of pristine FAPbI₃ slab with or without PTI. The formation energies of the aforementioned defects increase in the presence of PTI (Figure 3e); most notably, the formation energy of V_{FA} increases by 0.86 eV, indicating that PTI preferentially forms a strong binding with the undercoordinated surface FA⁺. Thus, PTI localized at the FAI terminated FAPbI₃ stabilizes the defective perovskite crystals by

forming additional hydrogen bonding with the undercoordinated surface FA^+ and suppresses the formation of vacancies and antisite defects.

Our defect passivated perovskite films with PTI were utilized to solar cells as a light absorber layer. The cross-sectional SEM image in Figure 4a shows the device structure with PTI-30 perovskite layer. Note that PTI nanosheets cannot be resolved here due to their thin thickness. Photovoltaic parameters from reverse scans were evaluated for 20 devices (Figure 4b and Figure S14). The PTI-30 PSCs lead to the highest performance with PCEs of $18.60 \pm 0.33\%$, substantially improved from the reference with PCEs of $16.59 \pm 0.20\%$ (12.1% enhancement). The fill factor (FF) increases modestly in PTI-30 PSCs (from $74.8 \pm 0.6\%$ to $77.2 \pm 0.6\%$), while a dramatic enhancement is found in the V_{oc} (from 1.03 ± 0.01 V to 1.12 ± 0.01 V). We attribute this improvement in the V_{oc} to the lower defect density in the perovskite film and stronger hole blocking between perovskite/ SnO_2 interfaces, as discussed earlier.⁴⁷ However, a further increase of PTI content (i.e., PTI-60) leads to the decrease in the overall photovoltaic parameters, particularly short-circuit current density (J_{sc}). This is attributed to the impeded charge collection across PTI and the subsequent decrease of electrical conductivity. The current density-voltage (J - V) curves of the champion devices from the references and PTI-30 are compared in Figure 4c and summarized in Table S2. The champion PTI-30 PSC shows a higher PCE of 19.10% (average value from reverse and forward scan results), compared to reference PSC (16.68%, 14.5% enhancement), principally benefiting from the enhanced V_{oc} (average V_{oc} from 1.03 V to 1.13 V). The PTI-30 device also exhibits the reduced J - V hysteresis suggesting that ion migration, commonly considered cause for J - V hysteresis, should be suppressed presumably due to the blocking of ion leakages through grain boundaries.⁵⁹ The integrated current density derived from

external quantum efficiency and the stabilized power output at maximum power point for the champion PTI-30 device are 21.04 mA/cm² and 18.82%, respectively, in a good agreement with the values obtained from the J - V curves (Figure S15).

For the systematic verification of the ion blocking effect by PTI, we examined the changes of current density in PSCs for 100 s upon biasing at different voltages (0.4 to 1.2 V with 0.4 V increments); the bias was switched off between the successive measurements (Figure 4d and S16).^{60, 61} The current density of the reference PSC continuously increased during each biasing step of 100 s, the rate of which became faster along with increasing voltage. This increase in the current density under a bias can be understood by an ion migration-induced reduction of built-in potential and the subsequent mitigation of the charge injection barrier in the device. Accordingly, the results from the reference reveal an undesirable ion migration. By contrast, the PTI-30 PSC presents more stable current densities, verifying the suppressed ion migration as consistent with the reduced J - V hysteresis. As discussed before, PTI tightly binds with the perovskite crystal surface via hydrogen bonding, so the 2D PTI with periodic electronegative functional groups can suppress ion migration via physically blocking the migration channel and/or electrostatic interaction with mobile ions.⁶²⁻⁶⁴ Noteworthy that while the PTI molecular structure contains intrinsic 12 Å nanopores, these electronegative cavities of the PTI electrostatically suppress the out-diffusion of halides and immobilize organic cations via hydrogen bonding.^{31, 65}

For a quantitative determination of defect densities with and without PTI, we utilized the space-charge-limited-current (SCLC) technique using electron-only devices of

ITO/SnO₂/perovskite/[6,6]-phenyl-C₆₁-butyric acid methyl ester/LiF/Au (Figure 4e).⁶⁰ Electron trap density (N_t) can be calculated from the following equation

$$V_{\text{TFL}} = \frac{eN_tL^2}{2\epsilon\epsilon_0}$$

where e is the elementary charge, L is the perovskite film thickness, ϵ is the relative permittivity (46.9)⁶⁶, ϵ_0 is the vacuum permittivity, and V_{TFL} is the trap-filling voltage. The electron trap density in the PTI-30 is estimated to be 8.51×10^{15} , about a half of the reference ($1.64 \times 10^{16} \text{ cm}^{-3}$). The passivation effect by PTI was further confirmed by reduced ideality factor (n_{id}), which was determined from the slope of V_{OC} vs. light intensity (Figure 4f). The calculated n_{id} decreases from 1.86 (the reference) to 1.44 (PTI-30), ensuring that defect-assisted recombination is largely suppressed in the perovskite layer.⁶⁷

Finally, we investigated the environmental stability of unencapsulated PSCs (reference and PTI-30), in humid air and under thermal stresses. As shown in Figure 4g and S17a, PTI-30 PSCs showed a markedly slow rate of the average PCE drop compared to reference PSCs during the storage under 25-45% humidity at room temperature. Thermal stability test was carried out at 85 °C under nitrogen atmosphere, and again PTI-30 PSCs exhibited a superior thermal stability than the reference PSCs (Figure 4h and S17b): after 500 h annealing, PTI-30 PSCs maintained ~80% of the initial PCE, while reference PSCs degraded below 50% of the initial efficiency. To identify the cause of enhanced thermal stability by PTI, XRD analysis was performed for the perovskite films after 250 h annealing (Figure S18). In the reference film, a strong new peak is emerged at 12.5° which is assigned to the (001) reflection of hexagonal PbI₂, resulting from the decomposition

of α -FAPbI₃ to PbI₂. Additionally, the peak from photoinactive hexagonal FAPbI₃ phase (δ -FAPbI₃) is observed.^{1, 68} In the case of PTI-30, the relative intensities of PbI₂ and δ -FAPbI₃ compared to α -FAPbI₃ are significantly lower than the reference PSC. The morphology of thermally aged perovskite films was analyzed by SEM (Figure S19). Insulating PbI₂ phases, hence appearing brighter in SEM imaging, are more prevalent in the reference. The improved thermal stability in the PTI-30 PSC is attributed to additional hydrogen bonding between PTI and undercoordinated surface organic cations that suppresses the thermal evaporation of volatile species and subsequent phase degradation.¹⁴

Conclusion

We have demonstrated that monodisperse 2D PTI nanosheets with dense surface functionalities and desirable electronic structure are highly effective for both chemical and electronic passivation of metal halide perovskites layers. PTI nanosheets provide the well-defined spatial distribution selectively localized at the defective interfaces and grain boundaries of the PSCs, thereby affording the reduced defect density in the perovskite films with the outstanding environmental stability originated from strong hydrogen bonding between the electronegative functional groups of PTI and undercoordinated organic cations at the surface of perovskite crystal. Additional benefits including the suppressed migration of mobile ions and electronically prevented hole quenching at the perovskite SnO₂ interfaces constitute the multifunctionality of PTI. The synergistic multifaceted benefits from PTI significantly improve the champion PSC efficiency (+14.5%) with respect to the reference device along with a negligible hysteresis. Moreover, non-encapsulated PTI-30 PSCs maintains ~80% of their initial PCEs after 500 h under the thermal stress of 85 °C, where the reference PSCs readily degraded. Our easy-to-implement passivation strategy is expected to be universally applicable to other hybrid PSCs and perovskite-based optoelectronic

devices, relying on common solution processing. This work suggests a new platform for judiciously designed 2D materials to suppress the undesired defect effects in the perovskite film and further improve the device performance and stability of the integrated PSCs.

Experimental Section

Materials.

Formamidinium iodide (FAI), methylammonium (MABr) were purchased from Dyesol, Lead iodide (PbI₂) and lead bromide (PbBr₂) were purchased from Tokyo Chemical Industry. Cesium iodide (CsI) and SnO₂ colloid precursor (tin IV) oxide, 15 wt% in H₂O colloidal dispersion) were purchased from Alfa Aesar. Anhydrous chlorobenzene, Acetonitrile, bis(trifluoromethane) sulfonamide lithium salt (LiTFSI), 4-*tert*-butylpyridine, anhydrous dimethyl sulfoxide (DMSO), anhydrous *N,N*-dimethylformamide (DMF), lithium bromide, potassium bromide, and dicyandiamide were purchased from Sigma Aldrich. Spiro-OMeTAD was purchased from Lumtec. Every chemical was used as received without further purification.

Synthesis of PTI

Bulk PTI powder was synthesized using the procedure of Miller *et al.*³⁰ and deintercalated using the procedure from Suter *et al.*³⁶ In short, dicyandiamide, lithium bromide, and potassium bromide were dried under vacuum and ground together in 1/2.6/2.4 weight ratio. The mixture was heated under a nitrogen flow to 400 °C for 1 h to partially crosslink the structure and limit pressure build up in the next step. The mixture was ground, sealed in a quartz ampule at $\sim 10^{-7}$ mbar, and heated to 600 °C for 16 h, before cooling, breaking open the ampule and washing the powder with

deionized water to remove exterior LiBr/KBr. The resultant brown powder of LiBr·PTI was then Soxhlet extracted with water for 3 days to give water-intercalated PTI.

Exfoliation of PTI

PTI dispersion was prepared by the spontaneous dissolution of PTI in polar aprotic solvents. Bulk PTI powder (10 mg) was weighed and finely grounded using a mortar. The resultant PTI powders were placed on glass vial and dried in a vacuum oven to remove residual water (150 °C at 10^{-3} mbar, 12 hours). Afterwards, the dried PTI powder was rapidly moved into a nitrogen-filled glovebox, where 8mL of DMF and 2mL of DMSO were added. Spontaneous exfoliation of PTI was induced in the DMF/DMSO mixed solvent (4:1/v:v) over 3 days, with by a mild agitation via occasional manual shaking. The resulting solution was filtered through a 0.2 μm PTFE syringe to remove aggregates, leaving a clear light yellow PTI dispersion, with the maximum concentration of $60 \pm 5 \mu\text{g/mL}$. For the calculation of the concentration of PTI dispersion, undissolved PTI parts was collected by filtration and washed by pure ethanol and then dried in a vacuum oven. The mass of dried undissolved PTI powder was weighed by a high sensitivity microgram balance. The concentration of PTI dispersion was obtained by subtracting the mass of undissolved PTI powder from the initial mass of PTI batch (10 mg).

PSCs fabrications

ITO glass was first cleaned successively with deionized water, ethanol, and IPA in an ultrasonic bath for 15 min each. The substrates were then dried in the oven and further cleaned by UV-Ozone (UVO) for 30 minutes. A thin film of SnO₂ was deposited on ITO glass substrate through spin coating a SnO₂ aqueous (2.67 wt%, from 15 wt% colloidal dispersion diluted with DI water 6.5:1 (v:v)). at 4000 rpm for 20 s followed by annealing at 150 °C for 30 minutes.

Immediately prior to perovskite film coating, the SnO₂ layer was treated by additional UVO for 45 minutes and moved into a nitrogen filled glovebox. For the fabrication of perovskite films, 1.1 M perovskite precursor solutions were created by combining CsI (0.07 M), FAI (1.1 M), MABr(0.22 M), PbI₂ (1.13 M) and PbBr₂ (0.23 M) in DMF:DMSO mixed solvent (4:1/v:v), creating a final perovskite with chemical formula Cs_{0.05}(FA_{0.85} MA_{0.15})Pb(I_{0.85}Br_{0.15})₃. For the PTI incorporated perovskite film (PTI-x), the PTI dispersion was directly used as the solvent for the perovskite precursor. PTI composition was predetermined by concentration of PTI in perovskite precursor. (Figure S3a). The perovskite precursor was spin casted in a two steps process at 1000 rpm for 10s and 6000 rpm for 25s respectively on the SnO₂ film. During the second step, 0.1 mL of chlorobenzene was dropped on the spinning substrate 5s prior to the end of the process. The substrates were immediately annealed at 100 °C for 45 minutes to achieve pin hole-free films. Next, a hole transport layer was fabricated by dynamic spin casting of spiro-OMeTAD solution (1 mL of chlorobenzene, 90.9 mg spiro-OMeTAD, 34.8 μL 4-*tert*-butylpyridine, 20.5 μL Li-TFSI (520 mg/ml in acetonitrile)). The spiro-OMeTAD solution was spin-coated at 2000 rpm for 20 s by dropping 20 μL of the solution on the spinning perovskite layer. The device was completed by thermal evaporation of an 80 nm gold layer with two step process: 2 nm at 0.1 Å/s and 78 nm at 1.2 Å/s.

PSCs characterization

Current density-voltage curves (*J-V*) of fabricated n-i-p solar cells were measured under a simulated AM 1.5G condition using a solar simulator (Newport, ORIEL, sol 1A) with a source meter (Keithley 2400). Before measuring PSCs, AM 1.5G irradiation was calibrated with a standard Si cell (Newport). A metal aperture with an area of 0.0675 cm² was used to define the active area of PSCs. Both reverse and forward *J-V* scan were performed by using a 100 mV/s with

a voltage step of 20 mV. EQE spectrum were measured by quantum efficiency measurements (PV Measurements QEX7) which were calibrated with a reference Si cell (PV measurements).

Device stability testing

For the aging tests under humidity, unencapsulated devices were stored in a desiccator under the dark at $25 \pm 3^\circ\text{C}$. During the aging period the relative humidity in the desiccator was controlled in the range of 25~45%. The thermal stability test was carried out in a N_2 glove box at 85°C where the encapsulated devices were aged. The photovoltaic performance of the aged devices were measured under ambient conditions. The polytriarylamine (PTAA, EM index) was used as the hole-transport material for the thermal stability test.

Perovskite film characterization

X-ray diffraction patterns were obtained from an X-ray diffractometer (XRD, D-Max 2200, Rigaku). Steady state PL spectra of the perovskite films were recorded with a monochromatic 633 nm laser by Raman/PL system (LabRAM HR Evolution Visible_NIR, HORIBA). Time-resolved PL spectra of perovskite layers were measured by a time correlated single photon spectroscopy (Fluorolog3, HORIBA). A DeltaDiode-470L laser (HORIBA) emitting pulsed laser (65 ps pulse width) at monochromatic 467 nm with a repetition rate of 80 MHz was used an excitation source. The excitation fluence is $4.0 \mu\text{J}/\text{cm}^2$ and the beam spot size is $\sim 2 \mu\text{m}$. The PL and TRPL measurements were carried out under ambient conditions for the unencapsulated samples. During the measurements, noticeable degradation of perovskite films was not detected. Absorption spectra of perovskite layer was recorded by UV-vis spectrometer (SolidSpec-3700, Shimadzu). UPS spectra was obtained using Micro X-Ray/UV Photoelectron Spectro microscopy (AXIS-NOVA, Kratos) with a He I (21.2 eV) source used as an excitation source. UPS samples were prepared on

ITO substrates to avoid the charging during measurements. The morphology analysis of perovskite films was performed by SEM (S-4800, Hitachi). Compositional depth profiling of perovskite films was carried out using a ToF-SIMS measurement (TOF-SIMS5, ION-TOF GmbH), operating with a 30 keV Bi³⁺ primary ion beam. For depth profiling, a 5 keV Ar cluster beam was used in order to minimize the sputter induced damage. The position of the SnO₂ substrate interface in the sputter depth profile defined by the maximum intensity of the SnO₂⁻ secondary ion.

¹H nuclear magnetic resonance (NMR)

The ¹H NMR spectra was conducted on an Agilent 400MHz 54mm NMR DD2 system. 10 mg of FAI in 1 ml of dimethyl sulfoxide-*d*₆ (DMSO-*d*₆) was used for the control sample. PTI dispersed in DMSO-*d*₆ synthesized using the same condition as for exfoliation of PTI, using pure DMSO-*d*₆ as solvent.

Attenuated total reflectance-Fourier transform infrared (ATR-FTIR)

The ATR-FTIR spectra were obtained from a Thermo Fisher Nicolet In 10MX purged by nitrogen gas. For the ATR-FTIR measurements, perovskite powders were prepared by scraping perovskite films fabricated with low perovskite precursor concentration (0.01 M) to increase the relative amount of PTI and enhance the PTI signal.

Transmission electron microscopic (TEM)

TEM analysis of PTI nanosheets was conducted using a Titan cubed G2 60-300 microscope (FEI) operated at 80 kV. A PTI dispersion (DMF/DMSO, 4:1) was drop casted and dried on the lacey carbon grids. An accelerating voltage of 300 kV, Tecnai G2 F30 S-Twin was used for confirming the incorporation of PTI in perovskite film (Figure 1c and d), PTI incorporated

perovskite films was scratched off from the substrate and dispersed in chloroform by sonication for 5 minutes, which was dropped on a lacy carbon grid.

Atomic Force Microscopy (AFM)

AFM measurements were conducted on a Park systems XE-100 operated in non-contact mode. For measuring the thickness of PTI, the samples were prepared by drop casting a drop of the PTI dispersion on the surface of silicon wafer, which was heated to 80 °C on a hot plate in order to evaporate the majority of the solvent.

Dynamic Light Scattering (DLS)

The dynamic light scattering (DLS) was measured using an Otsukael ELSZ-2000. The samples were prepared by dispersing 30 μL of the perovskite precursor solution into 3 mL of DMF:DMSO mixed solvent (4:1 v/v). PTI dispersed 3 mL of DMF:DMSO (4:1 v/v) was used for confirming the PTI dispersibility with perovskite colloidal precursor. The measurement was conducted with a quartz cuvette at 25 °C.

Computation details

The Density Functional Theory (DFT) calculation was performed using the Vienna Ab-initio Simulation Package (VASP). The exchange-correlation energy was described by using a generalized gradient approximation (GGA) with the Perdew-Burke-Ernzerhof (PBE) functional. The projector-augmented-wave (PAW) method with a plane wave up to an energy of 400 eV was used to treat ionic cores. The convergence criteria for ionic mean force and electronic structure were 0.03 eV/Å and 1.0×10^{-4} eV, respectively. The spin polarization and the dipole correction along the z direction were applied and the Van der Waals force was considered through the

Grimme's DFT-D3 method. The Brillouin zone was sampled using the Monkhorst-pack k-point mesh of $2 \times 2 \times 1$. The defect formation energy difference ($\Delta\Delta E_{defect}$) was calculated to estimate the effect of incorporation of PTI for stability. It was given by Equation (2) as follows:

$$\begin{aligned} \Delta\Delta E_{defect} &= \Delta E_{defect}[\text{PTI}] - \Delta E_{defect}[\text{ref}] \\ &= E_{defect}[\text{PTI}] - E_{pristine}[\text{PTI}] - E_{defect}[\text{ref}] + E_{pristine}[\text{ref}] \end{aligned} \quad (2)$$

Where $\Delta E_{defect}[\text{PTI}]$ and $\Delta E_{defect}[\text{ref}]$ are the defect formation energy in the presence of PTI and without PTI, respectively. $E_{defect}[\text{PTI}]$ and $E_{pristine}[\text{PTI}]$ are the total energies of the PTI-adsorbed surfaces with and without defect, respectively. $E_{defect}[\text{ref}]$ and $E_{pristine}[\text{ref}]$ are the total energies of the surfaces with and without defect, respectively.

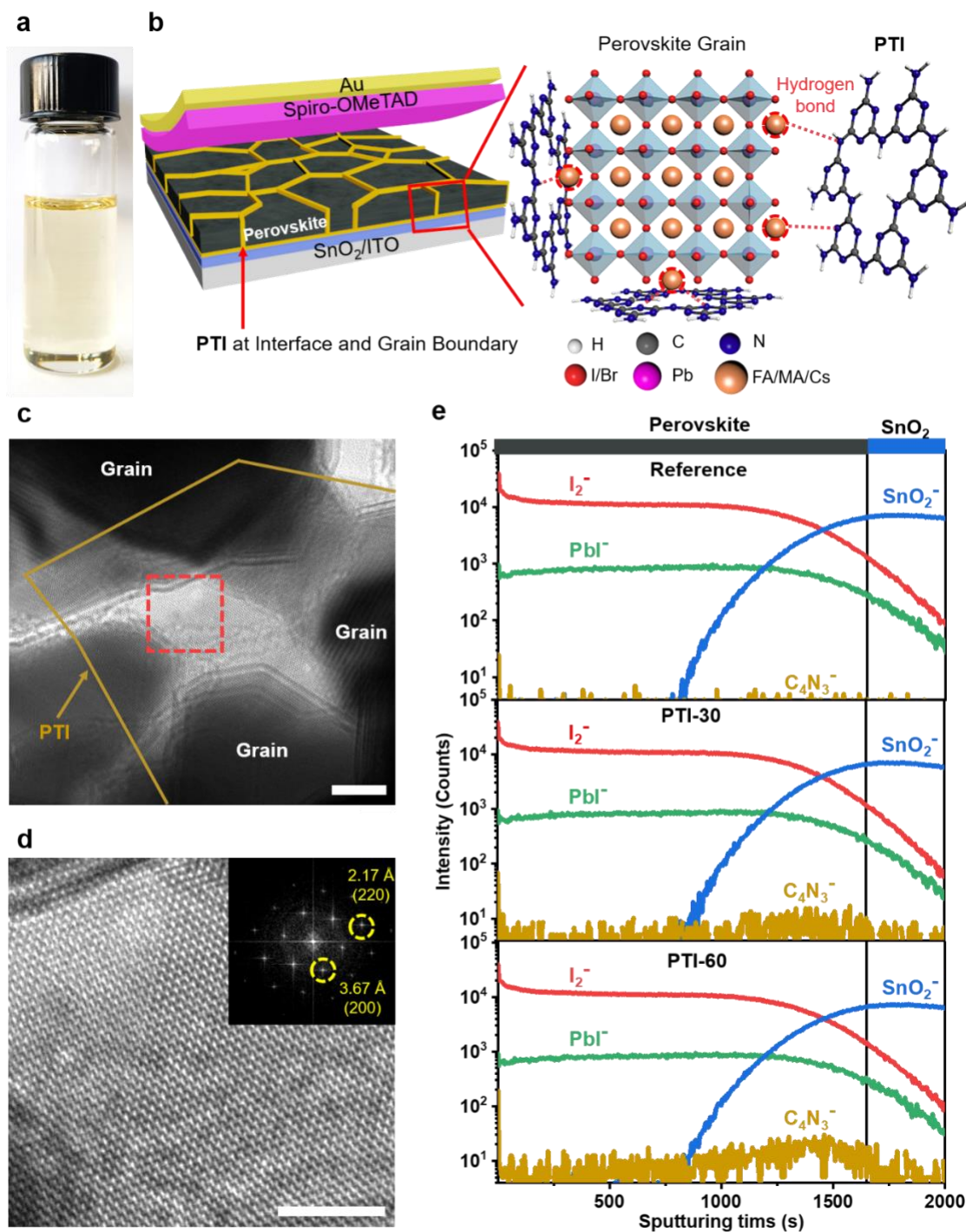


Figure 1. PTI-incorporated perovskite film. a) Photograph of PTI dispersion in DMF/DMSO solution, b) Schematic illustration of the device incorporating perovskite layer with PTI at interface and grain boundaries, c) High-resolution TEM images of the perovskite grain with PTI, d) Magnified TEM image of the regions highlighted with red dashed box in (c) and corresponding fast Fourier transform analysis of image, Scale bars (c) 10 and (d) 5 nm, e) ToF-SIMS depth profile analysis of reference, PTI-30 and PTI-60.

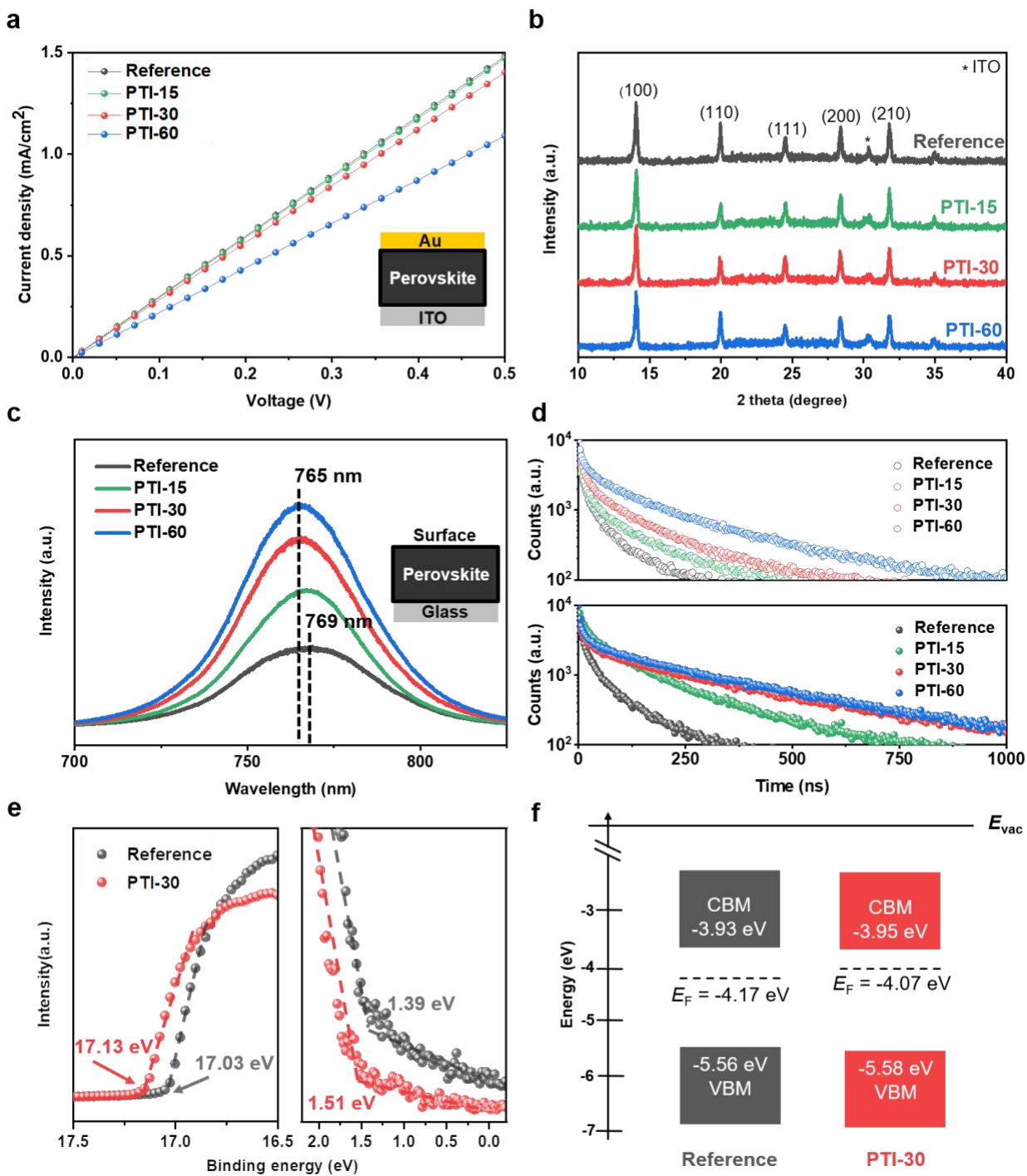


Figure 2. Effect of PTI incorporation on perovskite film. a) Vertical J-V curves of ITO/perovskites, b) X-ray diffraction patterns of perovskite films, c) Steady-state PL spectra of perovskite films excited by a 633 nm laser with incident light from the surface side, d) Time-resolved PL spectra of perovskite films excited by a 467 nm laser with incident light from the surface and glass sides. The excitation fluence is $4.0 \mu\text{J}/\text{cm}^2$ (repetition rate: 80 MHz), e) UPS spectra for the reference and PTI-30, f) Energy-level scheme for the reference and PTI-30 based on the parameters derived from UPS spectra in (e).

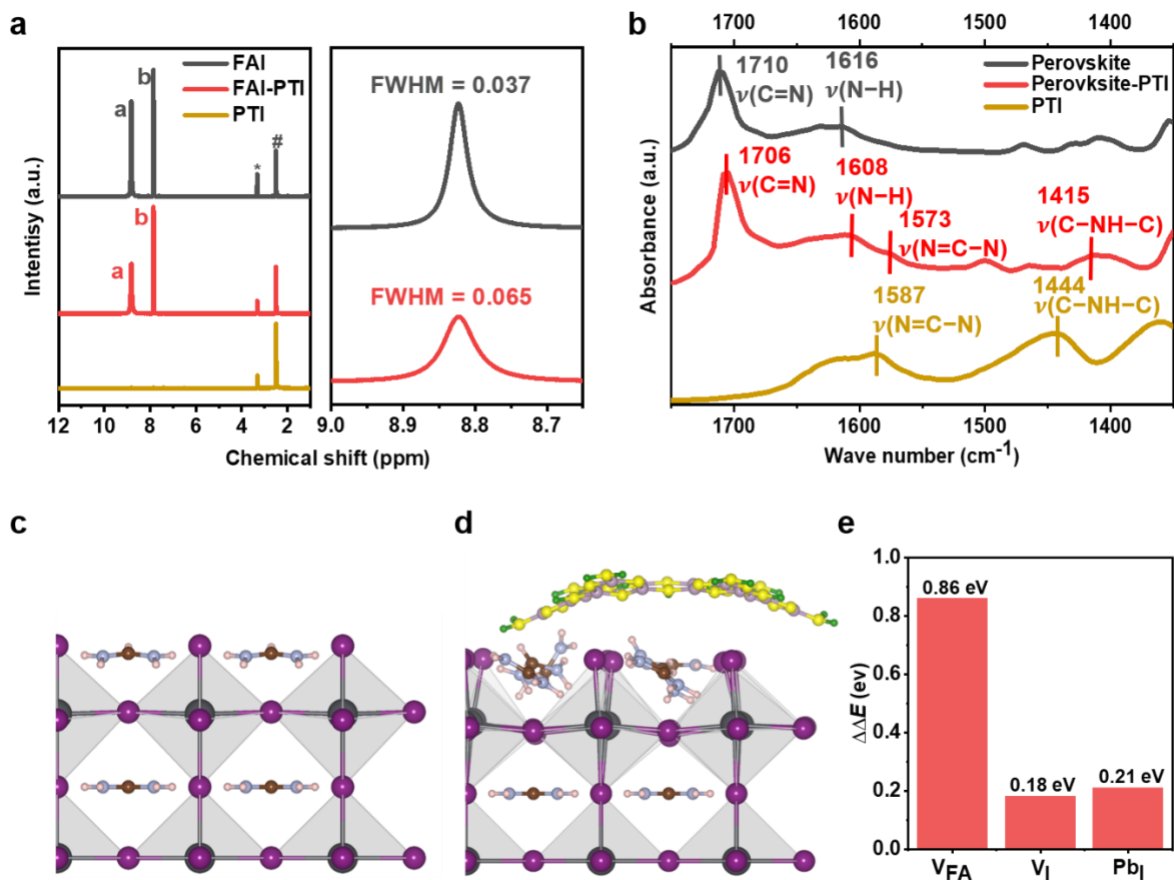


Figure 3. Interactions between PTI and perovskite. a) ^1H NMR spectra of FAI in $\text{DMSO-}d_6$, PTI dispersed $\text{DMSO-}d_6$ and FAI in PTI dispersed $\text{DMSO-}d_6$ (left) and magnified spectra in a chemical shift range of 8.65-9.0 ppm (right) (* and # represent the peak of water and DMSO respectively), b) FTIR spectra of perovskite, PTI and perovskite-PTI. FAI terminated FAPbI_3 (100) slab ($3\times 3\times 2$) without (c) and with PTI (d) (Pb [grey], I [purple], $\text{C}_{\text{perovskite}}$ [brown], $\text{N}_{\text{perovskite}}$ [blue], $\text{H}_{\text{perovskite}}$ [pink], C_{PTI} [mauve], N_{PTI} [yellow], and H_{PTI} [green]), e) Formation energy difference of vacancies and antisite defects at FAI terminated perovskite surface with PTI versus pure perovskite.

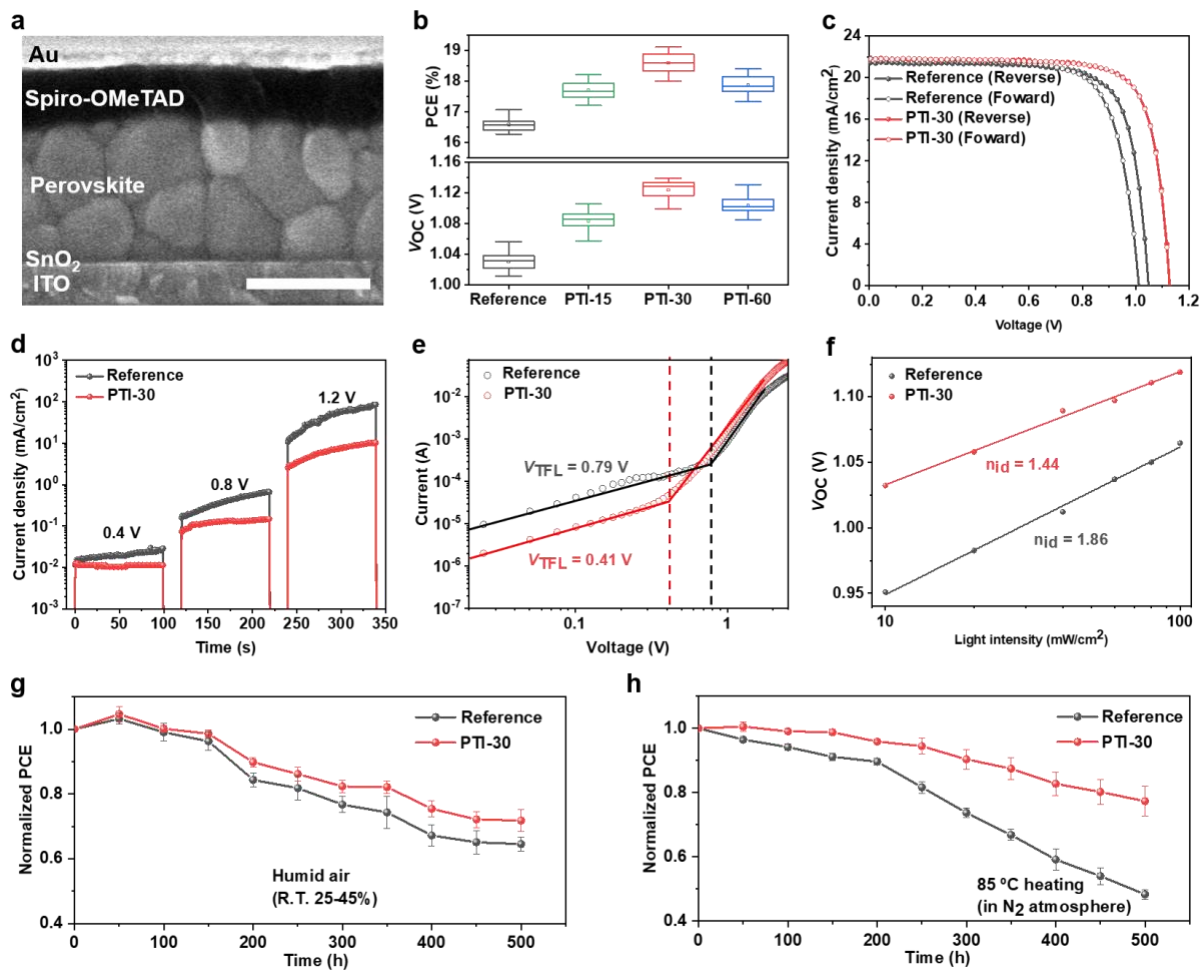


Figure 4. PTI effect on device performance and physics. a) Cross-sectional SEM image of PTI-30 (scale bar is 500 nm), b) Histograms of PCE and V_{oc} from corresponding PSCs measurements, c) Current density-voltage ($J-V$) curves of the reference and PTI-30 PSCs under AM 1.5G, d) Current behavior of perovskite solar cells under applied voltage in dark conditions, e) Space-charge-limited-current (SCLC) measurements of electron-only devices, f) Light-intensity dependent V_{oc} plots, Normalized PCEs evolution trends of aged devices at g) humid air (relative humidity of about 25-45%) and h) thermal stress (85 °C in a nitrogen atmosphere), In (g) and (h), the error bars represent the standard deviation for four devices.

Associated Content

Supporting Information.

Structure, Lateral size and Thickness of PTI, SIMS mass compound spectra of bulk PTI powder, UV-vis spectra, SEM images, PL spectra of perovskite films, ^1H NMR spectra of MABr, Histograms of J_{sc} and FF from corresponding PSCs measurements. EQE spectra, Stabilized power output, Dark currents of PSCs

Authors Information

Corresponding Author

* Corresponding Author: Adam J. Clancy (email: a.clancy@ucl.ac.uk), Byungha Shin (email: byungha@kaist.ac.kr), Sang Ouk Kim (email: sangouk.kim@kasit.ac.kr)

Notes

The authors declare no competing financial interest.

Acknowledgements

The DFT work was supported by the National Supercomputing Center with supercomputing resources including technical support (KSC-2020-CHA-0006). The author thanks the financial support from National Creative Research Initiative (CRI) Center for Multi-Dimensional Directed Nanoscale Assembly (2015R1A3A2033061).

Reference

1. Yoo, J. J.; Seo, G.; Chua, M. R.; Park, T. G.; Lu, Y.; Rotermund, F.; Kim, Y. K.; Moon, C. S.; Jeon, N. J.; Correa-Baena, J. P.; Bulovic, V.; Shin, S. S.; Bawendi, M. G.; Seo, J., Efficient Perovskite Solar Cells via Improved Carrier Management. *Nature* **2021**, *590* (7847), 587-593.
2. Jeon, T.; Jin, H. M.; Lee, S. H.; Lee, J. M.; Park, H. I.; Kim, M. K.; Lee, K. J.; Shin, B.; Kim, S. O., Laser Crystallization of Organic-Inorganic Hybrid Perovskite Solar Cells. *ACS Nano* **2016**, *10* (8), 7907-14.
3. Kim, D.; Jung, H. J.; Park, I. J.; Larson, B. W.; Dunfield, S. P.; Xiao, C.; Kim, M.; Kang, S. B.; Dravid, V.; Berry, J. J.; Kim, J. Y.; Zhu, K.; Kim, D. H.; Shin, B., Efficient, Stable Silicon Tandem Cells Enabled by Anion-Engineered Wide-Bandgap Perovskites. *Science* **2020**, *368*, 155-160.
4. Cho, H.; Jeong, S.-H.; Park, M.-H.; Kim, Y.-H.; Wolf, C.; Lee, C.-L.; Heo, J. H.; Sadhanala, A.; Myoung, N.; Yoo, S.; Im, S. H.; Friend, R. H.; Lee, T.-W., Overcoming the Electroluminescence Efficiency Limitations of Perovskite Light-Emitting Diodes. *Science* **2015**, *350* (6265), 1222-1225.
5. Jung, D. H.; Park, J. H.; Lee, H. E.; Byun, J.; Im, T. H.; Lee, G. Y.; Seok, J. Y.; Yun, T.; Lee, K. J.; Kim, S. O., Flash-Induced Ultrafast Recrystallization of Perovskite for Flexible Light-emitting Diodes. *Nano Energy* **2019**, *61*, 236-244.
6. Zhang, F.; Ma, Z.; Shi, Z.; Chen, X.; Wu, D.; Li, X.; Shan, C., Recent Advances and Opportunities of Lead-Free Perovskite Nanocrystal for Optoelectronic Application. *Energy Mater. Adv.* **2021**, *2021* (5198145), 1-38.
7. She, X.-J.; Chen, C.; Divitini, G.; Zhao, B.; Li, Y.; Wang, J.; Orri, J. F.; Cui, L.; Xu, W.; Peng, J.; Wang, S.; Sadhanala, A.; Siringhaus, H., A Solvent-based Surface Cleaning and Passivation Technique for Suppressing Ionic Defects in High-Mobility Perovskite Field-Effect Transistors. *Nat. Electron.* **2020**, *3* (11), 694-703.
8. Lee, G. Y.; Yang, M. Y.; Kim, D. H.; Lim, J.; Byun, J.; Choi, D. S.; Lee, H. J.; Nam, Y. S.; Kim, I. D.; Kim, S. O., Nitrogen-Dopant-Induced Organic-Inorganic Hybrid Perovskite Crystal Growth on Carbon Nanotubes. *Adv. Funct. Mater.* **2019**, *29* (30), 1902489.
9. NREL. Best Research-Cell Efficiency Chart. <https://www.nrel.gov/pv/cell-efficiency.html> (accessed 11 / 2021).
10. Leijtens, T.; Eperon, G. E.; Barker, A. J.; Grancini, G.; Zhang, W.; Ball, J. M.; Kandada, A. R. S.; Snaith, H. J.; Petrozza, A., Carrier Trapping and Recombination: The Role of Defect Physics in Enhancing the Open Circuit Voltage of Metal Halide Perovskite Solar Cells. *Energy Environ. Sci.* **2016**, *9* (11), 3472-3481.
11. Juarez-Perez, E. J.; Ono, L. K.; Qi, Y., Thermal Degradation of Formamidinium based Lead Halide Perovskites into Sym-triazine and Hydrogen Cyanide Observed by Coupled Thermogravimetry-Mass Spectrometry Analysis. *J. Mater. Chem. A* **2019**, *7* (28), 16912-16919.
12. Xue, J.; Wang, R.; Yang, Y., The Surface of Halide Perovskites from Nano to Bulk. *Nat. Rev. Mater.* **2020**, *5* (11), 809-827.
13. Eames, C.; Frost, J. M.; Barnes, P. R.; O'Regan, B. C.; Walsh, A.; Islam, M. S., Ionic Transport in Hybrid Lead Iodide Perovskite Solar Cells. *Nat. Commun.* **2015**, *6*, 7497.
14. Li, N.; Tao, S.; Chen, Y.; Niu, X.; Onwudinanti, C. K.; Hu, C.; Qiu, Z.; Xu, Z.; Zheng, G.; Wang, L.; Zhang, Y.; Li, L.; Liu, H.; Lun, Y.; Hong, J.; Wang, X.; Liu, Y.; Xie, H.; Gao, Y.; Bai, Y.; Yang, S.; Brocks, G.; Chen, Q.; Zhou, H., Cation and Anion Immobilization through Chemical Bonding Enhancement with Fluorides for Stable Halide Perovskite Solar Cells. *Nat.*

Energy **2019**, *4* (5), 408-415.

15. Wu, X.; Jiang, Y.; Chen, C.; Guo, J.; Kong, X.; Feng, Y.; Wu, S.; Gao, X.; Lu, X.; Wang, Q.; Zhou, G.; Chen, Y.; Liu, J. M.; Kempa, K.; Gao, J., Stable Triple Cation Perovskite Precursor for Highly Efficient Perovskite Solar Cells Enabled by Interaction with 18C6 Stabilizer. *Adv. Funct. Mater.* **2019**, *30* (6), 1908613.
16. Hanmandlu, C.; Swamy, S.; Singh, A.; Hsin-An, C.; Liu, C.-C.; Lai, C.-S.; Mohapatra, A.; Pao, C.-W.; Chen, P.; Chu, C.-W., Suppression of Surface Defects to Achieve Hysteresis-Free Inverted Perovskite Solar Cells via Quantum Dot Passivation. *J. Mater. Chem. A* **2020**, *8* (10), 5263-5274.
17. Han, T. H.; Lee, J. W.; Choi, C.; Tan, S.; Lee, C.; Zhao, Y.; Dai, Z.; De Marco, N.; Lee, S. J.; Bae, S. H.; Yuan, Y.; Lee, H. M.; Huang, Y.; Yang, Y., Perovskite-Polymer Composite Cross-Linker Approach for Highly-Stable and Efficient Perovskite Solar Cells. *Nat. Commun.* **2019**, *10* (1), 520.
18. Jiang, L.-L.; Wang, Z.-K.; Li, M.; Zhang, C.-C.; Ye, Q.-Q.; Hu, K.-H.; Lu, D.-Z.; Fang, P.-F.; Liao, L.-S., Passivated Perovskite Crystallization via g-C₃N₄ for High-Performance Solar Cells. *Adv. Funct. Mater.* **2018**, *28* (7), 1705875.
19. De Marco, N.; Zhou, H.; Chen, Q.; Sun, P.; Liu, Z.; Meng, L.; Yao, E. P.; Liu, Y.; Schiffer, A.; Yang, Y., Guanidinium: A Route to Enhanced Carrier Lifetime and Open-Circuit Voltage in Hybrid Perovskite Solar Cells. *Nano Lett.* **2016**, *16* (2), 1009-16.
20. Kim, Y.-H.; Kim, S.; Kakekhani, A.; Park, J.; Park, J.; Lee, Y.-H.; Xu, H.; Nagane, S.; Wexler, R. B.; Kim, D.-H.; Jo, S. H.; Martínez-Sarti, L.; Tan, P.; Sadhanala, A.; Park, G.-S.; Kim, Y.-W.; Hu, B.; Bolink, H. J.; Yoo, S.; Friend, R. H.; Rappe, A. M.; Lee, T.-W., Comprehensive Defect Suppression in Perovskite Nanocrystals for High-Efficiency Light-Emitting Diodes. *Nat. Photonics* **2021**, *15* (2), 148-155.
21. Su, T. S.; Eickemeyer, F. T.; Hope, M. A.; Jahanbakhshi, F.; Mladenovic, M.; Li, J.; Zhou, Z.; Mishra, A.; Yum, J. H.; Ren, D.; Krishna, A.; Ouellette, O.; Wei, T. C.; Zhou, H.; Huang, H. H.; Mensi, M. D.; Sivula, K.; Zakeeruddin, S. M.; Milic, J. V.; Hagfeldt, A.; Rothlisberger, U.; Emsley, L.; Zhang, H.; Gratzel, M., Crown Ether Modulation Enables over 23% Efficient Formamidinium-Based Perovskite Solar Cells. *J. Am. Chem. Soc.* **2020**, *142* (47), 19980-19991.
22. Bi, E.; Tang, W.; Chen, H.; Wang, Y.; Barbaud, J.; Wu, T.; Kong, W.; Tu, P.; Zhu, H.; Zeng, X.; He, J.; Kan, S.-i.; Yang, X.; Grätzel, M.; Han, L., Efficient Perovskite Solar Cell Modules with High Stability Enabled by Iodide Diffusion Barriers. *Joule* **2019**, *3* (11), 2748-2760.
23. Hadadian, M.; Correa-Baena, J. P.; Goharshadi, E. K.; Ummadisingu, A.; Seo, J. Y.; Luo, J.; Gholipour, S.; Zakeeruddin, S. M.; Saliba, M.; Abate, A.; Gratzel, M.; Hagfeldt, A., Enhancing Efficiency of Perovskite Solar Cells via N-doped Graphene: Crystal Modification and Surface Passivation. *Adv. Mater.* **2016**, *28* (39), 8681-8686.
24. Capasso, A.; Matteocci, F.; Najafi, L.; Prato, M.; Buha, J.; Cinà, L.; Pellegrini, V.; Carlo, A. D.; Bonaccorso, F., Few-Layer MoS₂ Flakes as Active Buffer Layer for Stable Perovskite Solar Cells. *Adv. Energy Mater.* **2016**, *6* (16), 1600920.
25. Liu, X.; Cheng, Y.; Tang, B.; Yu, Z. G.; Li, M.; Lin, F.; Zhang, S.; Zhang, Y.-W.; Ouyang, J.; Gong, H., Shallow Defects Levels and Extract Detrapped Charges to Stabilize Highly Efficient and Hysteresis-Free Perovskite Photovoltaic Devices. *Nano Energy* **2020**, *71*, 104556.
26. Agresti, A.; Pescetelli, S.; Palma, A. L.; Martín-García, B.; Najafi, L.; Bellani, S.; Moreels, I.; Prato, M.; Bonaccorso, F.; Di Carlo, A., Two-Dimensional Material Interface Engineering for Efficient Perovskite Large-Area Modules. *ACS Energy Lett.* **2019**, *4* (8), 1862-

1871.

27. Jin, X.; Yang, L.; Wang, X. F., Efficient Two-Dimensional Perovskite Solar Cells Realized by Incorporation of $\text{Ti}_3\text{C}_2\text{T}_x$ MXene as Nano-Dopants. *Nanomicro Lett.* **2021**, *13* (1), 68.
28. Wirnhier, E.; Doblinger, M.; Gunzelmann, D.; Senker, J.; Lotsch, B. V.; Schnick, W., Poly(triazine imide) with Intercalation of Lithium and Chloride Ions $[(\text{C}_3\text{N}_3)_2(\text{NH}(x)\text{Li}(1-x))_3\text{LiCl}]$: A Crystalline 2D Carbon Nitride Network. *Chem. Eur. J.* **2011**, *17* (11), 3213-21.
29. Miller, T. S.; Jorge, A. B.; Suter, T. M.; Sella, A.; Cora, F.; McMillan, P. F., Carbon Nitrides: Synthesis and Characterization of A New Class of Functional Materials. *Phys. Chem. Chem. Phys.* **2017**, *19* (24), 15613-15638.
30. Miller, T. S.; Suter, T. M.; Telford, A. M.; Picco, L.; Payton, O. D.; Russell-Pavier, F.; Cullen, P. L.; Sella, A.; Shaffer, M. S. P.; Nelson, J.; Tileli, V.; McMillan, P. F.; Howard, C. A., Single Crystal, Luminescent Carbon Nitride Nanosheets Formed by Spontaneous Dissolution. *Nano Lett.* **2017**, *17* (10), 5891-5896.
31. Clancy, A. J.; Suter, T. M.; Taylor, A.; Bhattacharya, S.; Miller, T. S.; Brázdová, V.; Aliev, A. E.; Chauvet, A. A. P.; Corà, F.; Howard, C. A.; McMillan, P. F., Understanding Spontaneous Dissolution of Crystalline Layered Carbon Nitride for Tuneable Photoluminescent Solutions and Glasses. *J. Mater. Chem. A* **2021**, *9* (4), 2175-2183.
32. Kessler, F. K.; Zheng, Y.; Schwarz, D.; Merschjann, C.; Schnick, W.; Wang, X.; Bojdys, M. J., Functional Carbon Nitride Materials — Design Strategies for Electrochemical Devices. *Nat. Rev. Mater.* **2017**, *2* (6), 17030.
33. Villalobos, L. F.; Vahdat, M. T.; Dakhchoune, M.; Nadizadeh, Z.; Mensi, M.; Oveisi, E.; Campi, D.; Marzari, N.; Agrawal, K. V., Large-Scale Synthesis of Crystalline g-C $_3$ N $_4$ Nanosheets and High-Temperature H $_2$ Sieving from Assembled Films. *Sci. Adv.* **2020**, *6*, eaay9851.
34. Li, X.-L.; Han, W.-P.; Wu, J.-B.; Qiao, X.-F.; Zhang, J.; Tan, P.-H., Layer-Number Dependent Optical Properties of 2D Materials and Their Application for Thickness Determination. *Adv. Funct. Mater.* **2017**, *27* (19), 1604468.
35. Kang, J.; Sangwan, V. K.; Wood, J. D.; Hersam, M. C., Solution-Based Processing of Monodisperse Two-Dimensional Nanomaterials. *Acc. Chem. Res.* **2017**, *50* (4), 943-951.
36. Suter, T. M.; Miller, T. S.; Cockcroft, J. K.; Aliev, A. E.; Wilding, M. C.; Sella, A.; Cora, F.; Howard, C. A.; McMillan, P. F., Formation of An Ion-Free Crystalline Carbon Nitride and its Reversible Intercalation with Ionic Species and Molecular Water. *Chem. Sci.* **2019**, *10* (8), 2519-2528.
37. Yasaei, P.; Kumar, B.; Foroozan, T.; Wang, C.; Asadi, M.; Tuschel, D.; Indacochea, J. E.; Klie, R. F.; Salehi-Khojin, A., High-Quality Black Phosphorus Atomic Layers by Liquid-Phase Exfoliation. *Adv. Mater.* **2015**, *27* (11), 1887-92.
38. Backes, C.; Smith, R. J.; McEvoy, N.; Berner, N. C.; McCloskey, D.; Nerl, H. C.; O'Neill, A.; King, P. J.; Higgins, T.; Hanlon, D.; Scheuschner, N.; Maultzsch, J.; Houben, L.; Duesberg, G. S.; Donegan, J. F.; Nicolosi, V.; Coleman, J. N., Edge and Confinement Effects Allow In Situ Measurement of Size and Thickness of Liquid-Exfoliated Nanosheets. *Nat. Commun.* **2014**, *5*, 4576.
39. Backes, C.; Szydłowska, B. M.; Harvey, A.; Yuan, S.; Vega-Mayoral, V.; Davies, B. R.; Zhao, P. L.; Hanlon, D.; Santos, E. J.; Katsnelson, M. I.; Blau, W. J.; Gadermaier, C.; Coleman, J. N., Production of Highly Monolayer Enriched Dispersions of Liquid-Exfoliated Nanosheets by Liquid Cascade Centrifugation. *ACS Nano* **2016**, *10* (1), 1589-601.
40. Yang, S.; Dai, J.; Yu, Z.; Shao, Y.; Zhou, Y.; Xiao, X.; Zeng, X. C.; Huang, J., Tailoring Passivation Molecular Structures for Extremely Small Open-Circuit Voltage Loss in Perovskite

Solar Cells. *J. Am. Chem. Soc.* **2019**, *141* (14), 5781-5787.

41. Wang, J.; Zhang, J.; Zhou, Y.; Liu, H.; Xue, Q.; Li, X.; Chueh, C. C.; Yip, H. L.; Zhu, Z.; Jen, A. K. Y., Highly Efficient All-Inorganic Perovskite Solar Cells with Suppressed Non-Radiative Recombination by A Lewis Base. *Nat. Commun.* **2020**, *11* (1), 177.

42. Zhao, Y.; Zhu, P.; Huang, S.; Tan, S.; Wang, M.; Wang, R.; Xue, J.; Han, T. H.; Lee, S. J.; Zhang, A.; Huang, T.; Cheng, P.; Meng, D.; Lee, J. W.; Marian, J.; Zhu, J.; Yang, Y., Molecular Interaction Regulates the Performance and Longevity of Defect Passivation for Metal Halide Perovskite Solar Cells. *J. Am. Chem. Soc.* **2020**, *142* (47), 20071-20079.

43. Han, Q.; Bai, Y.; Liu, J.; Du, K.-z.; Li, T.; Ji, D.; Zhou, Y.; Cao, C.; Shin, D.; Ding, J.; Franklin, A. D.; Glass, J. T.; Hu, J.; Therien, M. J.; Liu, J.; Mitzi, D. B., Additive Engineering for High-Performance Room-Temperature-Processed Perovskite Absorbers with Micron-Size Grains and Microsecond-Range Carrier Lifetimes. *Energy & Environmental Science* **2017**, *10* (11), 2365-2371.

44. De Wolf, S.; Holovsky, J.; Moon, S. J.; Loper, P.; Niesen, B.; Ledinsky, M.; Haug, F. J.; Yum, J. H.; Ballif, C., Organometallic Halide Perovskites: Sharp Optical Absorption Edge and Its Relation to Photovoltaic Performance. *J. Phys. Chem. Lett.* **2014**, *5* (6), 1035-9.

45. Shao, Y.; Xiao, Z.; Bi, C.; Yuan, Y.; Huang, J., Origin and Elimination of Photocurrent Hysteresis by Fullerene Passivation in CH₃NH₃PbI₃ Planar Heterojunction Solar Cells. *Nat. Commun.* **2014**, *5*, 5784.

46. Agresti, A.; Pazniak, A.; Pescetelli, S.; Di Vito, A.; Rossi, D.; Pecchia, A.; Auf der Maur, M.; Liedl, A.; Larciprete, R.; Kuznetsov, D. V.; Saranin, D.; Di Carlo, A., Titanium-Carbide MXenes for Work Function and Interface Engineering in Perovskite Solar Cells. *Nat. Mater.* **2019**, *18* (11), 1228-1234.

47. Zheng, X.; Hou, Y.; Bao, C.; Yin, J.; Yuan, F.; Huang, Z.; Song, K.; Liu, J.; Troughton, J.; Gasparini, N.; Zhou, C.; Lin, Y.; Xue, D.-J.; Chen, B.; Johnston, A. K.; Wei, N.; Hedhili, M. N.; Wei, M.; Alsalloum, A. Y.; Maity, P.; Turedi, B.; Yang, C.; Baran, D.; Anthopoulos, T. D.; Han, Y.; Lu, Z.-H.; Mohammed, O. F.; Gao, F.; Sargent, E. H.; Bakr, O. M., Managing Grains and Interfaces via Ligand Anchoring Enables 22.3%-Efficiency Inverted Perovskite Solar Cells. *Nat. Energy* **2020**, *5* (2), 131-140.

48. Li, F.; Deng, X.; Qi, F.; Li, Z.; Liu, D.; Shen, D.; Qin, M.; Wu, S.; Lin, F.; Jang, S. H.; Zhang, J.; Lu, X.; Lei, D.; Lee, C. S.; Zhu, Z.; Jen, A. K., Regulating Surface Termination for Efficient Inverted Perovskite Solar Cells with Greater Than 23% Efficiency. *J. Am. Chem. Soc.* **2020**, *142* (47), 20134-20142.

49. Wu, W. Q.; Liao, J. F.; Zhong, J. X.; Xu, Y. F.; Wang, L.; Huang, J., Suppressing Interfacial Charge Recombination in Electron-Transport-Layer-Free Perovskite Solar Cells to Give an Efficiency Exceeding 21. *Angew. Chem. Int. Ed.* **2020**, *59* (47), 20980-20987.

50. Chen, R.; Long, B.; Wang, S.; Liu, Y.; Bai, J.; Huang, S.; Li, H.; Chen, X., Efficient and Stable Perovskite Solar Cells Using Bathocuproine Bilateral-Modified Perovskite Layers. *ACS Appl. Mater. Interfaces* **2021**, *13* (21), 24747-24755.

51. Lee, Y.; Paek, S.; Cho, K. T.; Oveisi, E.; Gao, P.; Lee, S.; Park, J.-S.; Zhang, Y.; Humphry-Baker, R.; Asiri, A. M.; Nazeeruddin, M. K., Enhanced Charge Collection with Passivation of the Tin Oxide Layer in Planar Perovskite Solar Cells. *J. Mater. Chem. A* **2017**, *5* (25), 12729-12734.

52. Chen, Q.; Zhou, H.; Song, T. B.; Luo, S.; Hong, Z.; Duan, H. S.; Dou, L.; Liu, Y.; Yang, Y., Controllable Self-Induced Passivation of Hybrid Lead Iodide Perovskites Toward High Performance Solar Cells. *Nano Lett.* **2014**, *14* (7), 4158-63.

53. Xu, W.; Hu, Q.; Bai, S.; Bao, C.; Miao, Y.; Yuan, Z.; Borzda, T.; Barker, A. J.; Tyukalova, E.; Hu, Z.; Kawecki, M.; Wang, H.; Yan, Z.; Liu, X.; Shi, X.; Uvdal, K.; Fahlman, M.; Zhang, W.; Duchamp, M.; Liu, J.-M.; Petrozza, A.; Wang, J.; Liu, L.-M.; Huang, W.; Gao, F., Rational Molecular Passivation for High-Performance Perovskite Light-Emitting Diodes. *Nat. Photonics* **2019**, *13* (6), 418-424.
54. Dong, Q.; Zhu, C.; Chen, M.; Jiang, C.; Guo, J.; Feng, Y.; Dai, Z.; Yadavalli, S. K.; Hu, M.; Cao, X.; Li, Y.; Huang, Y.; Liu, Z.; Shi, Y.; Wang, L.; Padture, N. P.; Zhou, Y., Interpenetrating Interfaces for Efficient Perovskite Solar Cells with High Operational Stability and Mechanical Robustness. *Nat. Commun.* **2021**, *12* (1), 973.
55. Chong, S. Y.; Jones, J. T. A.; Khimiyak, Y. Z.; Cooper, A. I.; Thomas, A.; Antonietti, M.; Bojdys, M. J., Tuning of Gallery Heights in A Crystalline 2D Carbon Nitride Network. *J. Mater. Chem. A* **2013**, *1* (4), 1102-1107.
56. Gallo, M.; Matteucci, S.; Alaimo, N.; Pitti, E.; Orsale, M. V.; Summa, V.; Cicero, D. O.; Monteagudo, E., A Novel Method Using Nuclear Magnetic Resonance for Plasma Protein Binding Assessment in Drug Discovery Programs. *J. Pharm. Biomed. Anal.* **2019**, *167*, 21-29.
57. Tan, S.; Huang, T.; Yavuz, I.; Wang, R.; Weber, M. H.; Zhao, Y.; Abdelsamie, M.; Liao, M. E.; Wang, H. C.; Huynh, K.; Wei, K. H.; Xue, J.; Babbe, F.; Goorsky, M. S.; Lee, J. W.; Sutter-Fella, C. M.; Yang, Y., Surface Reconstruction of Halide Perovskites During Post-treatment. *J. Am. Chem. Soc.* **2021**, *143* (18), 6781-6786.
58. Quarti, C.; De Angelis, F.; Beljonne, D., Influence of Surface Termination on the Energy Level Alignment at the CH₃NH₃PbI₃ Perovskite/C₆₀ Interface. *Chem. Mater.* **2017**, *29* (3), 958-968.
59. Lee, J.-W.; Kim, S.-G.; Yang, J.-M.; Yang, Y.; Park, N.-G., Verification and Mitigation of Ion Migration in Perovskite Solar Cells. *APL Mater.* **2019**, *7* (4), 041111.
60. Kim, H.; Kim, J. S.; Heo, J. M.; Pei, M.; Park, I. H.; Liu, Z.; Yun, H. J.; Park, M. H.; Jeong, S. H.; Kim, Y. H.; Park, J. W.; Oveisi, E.; Nagane, S.; Sadhanala, A.; Zhang, L.; Kweon, J. J.; Lee, S. K.; Yang, H.; Jang, H. M.; Friend, R. H.; Loh, K. P.; Nazeeruddin, M. K.; Park, N. G.; Lee, T. W., Proton-Transfer-Induced 3D/2D Hybrid Perovskites Suppress Ion Migration and Reduce Luminance Overshoot. *Nat. Commun.* **2020**, *11* (1), 3378.
61. Ma, Y.; Cheng, Y.; Xu, X.; Li, M.; Zhang, C.; Cheung, S. H.; Zeng, Z.; Shen, D.; Xie, Y. M.; Chiu, K. L.; Lin, F.; So, S. K.; Lee, C. S.; Tsang, S. W., Suppressing Ion Migration Across Perovskite Grain Boundaries by Polymer Additives. *Adv. Funct. Mater.* **2020**, *31* (3), 2006802.
62. Bi, E.; Chen, H.; Xie, F.; Wu, Y.; Chen, W.; Su, Y.; Islam, A.; Gratzel, M.; Yang, X.; Han, L., Diffusion Engineering of Ions and Charge Carriers for Stable Efficient Perovskite Solar Cells. *Nat. Commun.* **2017**, *8*, 15330.
63. Fan, W.; Zhang, S.; Xu, C.; Si, H.; Xiong, Z.; Zhao, Y.; Ma, K.; Zhang, Z.; Liao, Q.; Kang, Z.; Zhang, Y., Grain Boundary Perfection Enabled by Pyridinic Nitrogen Doped Graphdiyne in Hybrid Perovskite. *Adv. Funct. Mater.* **2021**, *31* (34), 2104633.
64. Li, M.; Zuo, W. W.; Wang, Q.; Wang, K. L.; Zhuo, M. P.; Köbler, H.; Halbig, C. E.; Eigler, S.; Yang, Y. G.; Gao, X. Y.; Wang, Z. K.; Li, Y.; Abate, A., Ultrathin Nanosheets of Oxofunctionalized Graphene Inhibit the Ion Migration in Perovskite Solar Cells. *Adv. Energy Mater.* **2019**, *10* (4), 1902653.
65. Foglia, F.; Clancy, A. J.; Berry-Gair, J.; Lisowska, K.; Wilding, M. C.; Suter, T. M.; Miller, T. S.; Smith, K.; Demmel, F.; Appel, M.; Sakai, V. G.; Sella, A.; Howard, C. A.; Tyagi, M.; Corà, F.; McMillan, P. F., Aquaporin-Like Water Transport in Nanoporous Crystalline Layered Carbon Nitride. *Sci. Adv.* **2020**, *6*, eabb6011.

66. Han, Q.; Bae, S. H.; Sun, P.; Hsieh, Y. T.; Yang, Y. M.; Rim, Y. S.; Zhao, H.; Chen, Q.; Shi, W.; Li, G.; Yang, Y., Single Crystal Formamidinium Lead Iodide (FAPbI₃): Insight into the Structural, Optical, and Electrical Properties. *Adv. Mater.* **2016**, *28* (11), 2253-8.
67. Jiang, Q.; Zhao, Y.; Zhang, X.; Yang, X.; Chen, Y.; Chu, Z.; Ye, Q.; Li, X.; Yin, Z.; You, J., Surface Passivation of Perovskite Film for Efficient Solar Cells. *Nat. Photonics* **2019**, *13* (7), 460-466.
68. Wang, R.; Xue, J.; Meng, L.; Lee, J.-W.; Zhao, Z.; Sun, P.; Cai, L.; Huang, T.; Wang, Z.; Wang, Z.-K.; Duan, Y.; Yang, J. L.; Tan, S.; Yuan, Y.; Huang, Y.; Yang, Y., Caffeine Improves the Performance and Thermal Stability of Perovskite Solar Cells. *Joule* **2019**, *3* (6), 1464-1477.

TOC GRAPHICS

